LA-UR-21-23236 (Accepted Manuscript)

P–V–T Equation of State of Iridium Up to 80 GPa and 3100 K

Burakovsky, Leonid
Anzellini, Simone
Turnbull, Robin
Bandiello, Enrico
Errandonea, Daniel

To be published in: Crystals

DOI to publisher's version: 10.3390/cryst11040452

Permalink to record: http://permalink.lanl.gov/object/view?what=info:lanl-repo/lareport/LA-UR-21-23236 crystals

Article

P–V–T Equation of State of Iridium Up to 80 GPa and 3100 K

Simone Anzellini [1,*], Leonid Burakovsky [2], Robin Turnbull [3], Enrico Bandiello [3] and Daniel Errandonea [3]

[1] Diamond Light Source Ltd., Harwell Science & Innovation Campus, Diamond House, Didcot OX11 0DE, UK
[2] Los Alamos National Laboratory, Theoretical Divisions, Los Alamos, NM 87545, USA; burakov@lanl.gov
[3] Departamento de Física Aplicada-Instituto de Ciencia de Materiales, Matter at High Pressure (MALTA) Consolider Team, Universidad de Valencia, Edificio de Investigación, C/Dr. Moliner 50, Burjassot, 46100 Valencia, Spain; robin.turnbull@uv.es (R.T.); enrico.bandiello@uv.es (E.B.); daniel.errandonea@uv.es (D.E.)
* Correspondence: simone.anzellini@diamond.ac.uk

Abstract: In the present study, the high-pressure high-temperature equation of the state of iridium has been determined through a combination of in situ synchrotron X-ray diffraction experiments using laser-heating diamond-anvil cells (up to 48 GPa and 3100 K) and density-functional theory calculations (up to 80 GPa and 3000 K). The melting temperature of iridium at 40 GPa was also determined experimentally as being 4260 (200) K. The results obtained with the two different methods are fully consistent and agree with previous thermal expansion studies performed at ambient pressure. The resulting thermal equation of state can be described using a third-order Birch–Murnaghan formalism with a Berman thermal-expansion model. The present equation of the state of iridium can be used as a reliable primary pressure standard for static experiments up to 80 GPa and 3100 K. A comparison with gold, copper, platinum, niobium, rhenium, tantalum, and osmium is also presented. On top of that, the radial-distribution function of liquid iridium has been determined from experiments and calculations.

Keywords: iridium; equation of state; high pressure; X-ray diffraction; laser heating; density-functional theory; melting; radial-distribution function

Citation: Anzellini, S.; Burakovsky, L.; Turnbull, R.; Bandiello, E.; Errandonea, D. P-V-T Equation of State of Iridium Up to 80 GPa and 3100 K. *Crystals* **2021**, *11*, 452. https://doi.org/10.3390/cryst11040452

Academic Editor: Shujun Zhang

Received: 30 March 2021
Accepted: 15 April 2021
Published: 20 April 2021

1. Introduction

Iridium (Ir) belongs to the family of the 5d transition metals. It exhibits a face-centered cubic (fcc) structure and its electronic structure is [Xe] $4f^{14}\ 5d^7\ 6s^2$. Similar to the other elements of the $5d$ family (such as Re, W, Pt, and Ta), Ir has always attracted considerable interest in the scientific community due to its outstanding mechanical and thermal properties. In particular, Ir is the most commonly used metal in high-temperature (HT) crucibles, thermocouples, and encapsulators of nuclear-powered electrical generators in space technology. Furthermore, thanks to its high shear modulus, chemical inertness, refractory nature, and phase stability, Ir is ideally suited as gasket material in static experiments in diamond-anvil cells (DAC) or as pressure standard for high-pressure (HP) experiments (in both static and dynamic experiments). As it exhibits excellent mechanical properties and high resistance to oxidation and corrosion at elevated temperature, Ir is also used in numerous applications as a static component at high T and/or in aggressive environments. In particular, Ir is notably inert in comparison to other transition metals [1], and it is largely immune to chemical reactions in comparison to refractory metals such as rhenium [2] or tungsten [3].

Despite the multiple technological applications of Ir, our current understanding of its mechanical properties is rather limited and knowledge of its HP–HT phase diagram is virtually non-existent. In particular, a solid–solid phase transition was observed in shock-wave experiments [4] to occur between 140 and 180 GPa. In a previous DAC experiment, performed under non-hydrostatic conditions using energy-dispersive X-ray diffraction

(XRD), a distortion of the *fcc* lattice was observed at room temperature (*RT*) and 59 GPa [5] and interpreted as a formation of a complex super-lattice. However, no phase transition was observed at *RT* in a recent DAC experiment performed under hydrostatic conditions (using helium as pressure medium) up to 140 GPa using angular-dispersive XRD [1]. A phase transition has been predicted to happen at 2000 K and 150 GPa from a *fcc* phase to a disordered hexagonal close-packed phase (*rhcp*) by a recent theoretical study [6] based on ab initio simulations.

An additional interest in iridium was generated by predicted structural anomalies attributed to an unusual electronic transition called core-level crossing (CLC). In fact, it is known that electronic transitions are expected to strongly affect material properties, such as elastic moduli, thermal expansion, resistivity and thermal conductivity. Such an electronic transition has been recently observed for the first time in a double-staged DAC study of osmium (another 5d metal), which compressed up to 770 GPa [7]. In particular, the CLC electronic transition was correlated to a discontinuity in the measured c/a axial ratio of the Os *hcp* structure at 440 GPa. Consequently, systematic theoretical studies have been conducted to predict possible CLC transitions for all of the 5d transition metals. In the case of Ir, such a transition was predicted to occur at 80 GPa [8]. However, a recent X-ray absorption near-edge structure (XANES) experiment that aimed to obtain information on the electronic structural evolution of Ir up to 90 GPa could not find any evidence of any CLC transition [1].

It is therefore evident that an in-depth characterization of the structural and physical properties of Ir at *HP* and *HT* conditions is still lacking. In the present work, the structural evolution of Ir has been characterized up to 80 GPa and 4260 K through a combination of in situ powder X-ray diffraction experiments and density-functional theory (DFT) calculations. In particular, the structural domain of solid Ir (always *fcc*) in the investigated *P*-*T* range, the melting point at 40.3 GPa, the radial-distribution function (RDF) of liquid Ir, and the corresponding thermal equation of state (EoS) have all been established.

2. Materials and Methods

2.1. Experimental Details

Two membrane DACs with diamonds of culet sizes of 400 µm and 300 µm were equipped with pre-indented and spark-erosion drilled Re gaskets. In order to prevent any oxidation, the sample preparation and loading was performed in a glovebox under an argon atmosphere. Samples were obtained from Ir powder sourced from Goodfellow (99.9% purity). Grains of the powder sample were compressed between two diamond anvils in order to create a foil. The obtained foil was then cut and loaded in the DAC high-pressure chambers (see Figure 1) between two magnesium oxide (MgO) disks (99.9% purity). The MgO, acting as insulating material (both thermally and chemically) as well as pressure gauge, was oven dried at 200 °C for two hours before being loaded in the DAC to remove any water or moisture.

Angular-dispersive powder XRD patterns were collected at the extreme conditions beamline, I15, of the Diamond Light Source [9]. The polychromatic beam of the I15's wiggler was tuned to 29.5 keV and focused down to 6×9 µm^2 (full-width at half maximum (FWHM)). A Pilatus 2M detector was used to ensure fast data collections with a good signal/noise ratio. The sample-to-detector distance was measured following the standard procedure from the diffraction rings of a CeO_2 sample.

The loaded DACs were mounted on the laser-heating (LH) system of I15 [9]. Each heating ramp was performed at a selected initial *P*. The sample inside the DAC was heated in double-sided mode [10]. Before each heating ramp, the two Nd:YAG fiber lasers were individually focused on the sample surface and their power was linearly increased until a clear hot spot was observed on the camera. During the laser alignment procedure, the exposure time of the cameras was maximized to be able to observe the hot spot at a relatively "low *T*" (around 1000 K). In this way, it was possible to avoid any unwanted damage of the sample. Furthermore, in order to prevent the X-ray beam from sampling a radial T gradient on the sample surface, the two lasers were intentionally slightly unfocused to maximize the size of the hot spot at uniform T. Finally, the lasers were coupled together and their relative positions were tuned to obtain a uniform hot spot of around 30 µm in diameter.

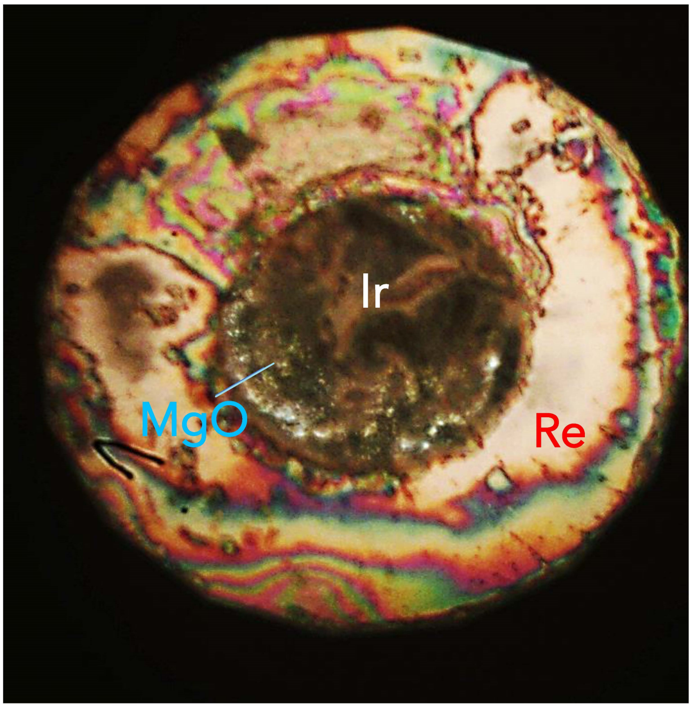

Figure 1. Photograph of the DAC high-pressure chamber after sample loading at ambient conditions. Despite the opacity of MgO, it is possible to observe the Ir embedded on it. The external ring is the Re gasket.

During the experiments, the T on both sides of the sample was measured by spectral radiometry following the procedure described in Benedetti and Loubeyre [11]. The error in the T measurements was calculated as the maximum values between the difference in the T measured on each side of the sample and the FWHM of the histogram of the two-colours pyrometry [10]. The P experienced by the sample was measured from the thermal EoS of MgO [12] (under the assumption of Ir and MgO being at the same T) using the measured volume of MgO and the average between the T measured from both sides of the sample. The errors in P measurement were estimated to be of the order of 5 GPa at 1500 K and of 7.5 GPa at 4260 K (the highest T reached in the present experiment). Such an estimation was obtained considering the adopted MgO thermal EoS [12] and the thermal gradient developed in the DAC high pressure chamber (therefore, inside the MgO), ranging from the measured T to 300 K at the interface with the diamonds. Before and after each heating ramp, the relative alignment of the X-rays with the lasers and the T reading were checked following the procedure described in Anzellini et al. [13]

In order to minimize the laser–sample interaction time (therefore, minimizing possible chemical reactions and sample damaging), the heating ramps were performed in a "trigger mode"; i.e., both lasers were set to a target power, after 0.3 s, a diffraction pattern and a temperature measurement were collected simultaneously. Then, 0.3 s after the XRD collection, both lasers were turned off synchronously. The XRD collection time was set to 1 s, whereas the acquisition time for the T measurements was adjusted according to the signal saturation.

During each run, the target power of the lasers was increased until a diffuse ring (characteristic of a liquid sample) was detected in the diffraction pattern or it was not possible to increase T any further. An accurate analysis of the diffraction patterns was performed in order to detect the appearance of the melting and to obtain structural and textural information about the sample and the insulating material. During the analysis procedure, masks were applied on a per-image basis using the DIOPTAS suite [14]. The images were azimuthally integrated and a LeBail analysis was performed using the TOPAS suite [15] software in order to identify crystal structures and determine unit–cell parameters at different P–T conditions. The EosFit suite [16] was used to determine the corresponding thermal EoS from the obtained data. The melting at HP was determined by the appearance of a diffuse scattering in the Ir diffraction signal.

2.2. Computational Methods

Calculations were performed using a quantum molecular dynamic (QMD) code and the Vienna Ab initio Simulation Package (VASP) based on DFT. In particular, for the present simulations of the equation of state of iridium, we used the local-density approximation (LDA). The success of LDA applied to materials as dense as Ir was demonstrated with the example of gold [17]. At low temperatures, the LDA error shifts the lattice constants towards smaller values, but this shift appears to be very negligible for high density materials. At these lattice constants the thermal pressure has a negligible volume dependence, and, therefore, the effect of the LDA error is small. This explains why LDA is very successful when applied to denser materials at low T. The absolute volume dependence of the thermal pressure is rather similar for both LDA and its alternative generalized-gradient approximation (GGA), and both show strongly increasing thermal pressure at larger volumes. However, as the volume decreases (with increasing pressure), the LDA increase of thermal pressure slows down, which causes LDA to deteriorate at smaller volumes and higher temperatures. This will be discussed when comparing DFT results on Ir with the experiments.

Ir was modeled by placing its nine outermost electrons ($5d^7\ 6s^2$) to the valence. These nine valence electrons were represented with a plane-wave basis set with cutoff energy of 300 eV, while the core electrons were represented by projector augmented-wave (PAW) pseudo potentials. A $2 \times 2 \times 2$ (32-atoms) super-cell was used in each case, with a very dense k-point mesh of $35 \times 35 \times 35$; this choice ensures full-energy convergence better than 0.1 meV/atom, which was checked for each run. For finite-T simulations, we used the algorithm of Nosé, which induces temperature fluctuations of approximately the same frequency as the typical phonon frequencies of the material at the simulated P–T conditions. The finite-T simulations typically require between 7500 and 10,000 time steps (of 1 fs) to achieve full energy convergence and to produce sufficiently long output for the extraction of reliable average for the value of pressure. An example of the time evolution of both temperature and pressure during a Nosé algorithm run is shown in Figure 2.

To calculate the theoretical RDF of liquid Ir, we first prepared a liquid by melting fcc-Ir. To this end, we used a $4 \times 4 \times 4$ (256 atoms) fcc-Ir super-cell with a lattice constant of 4.0 Å, which was subject to initial T of 20,000 K and NVE-run for 10 ps (NVE means we used a micro-canonical ensemble in which the total number of particles (N), the volume (V), and the total energy (E) are assumed to be constant in the ensemble). The emerging liquid that reached equilibrium at $T \approx 8000$ K was slowly cooled down to 4260 K. The size of the liquid super-cell was slightly decreased to correspond to ≈40 GPa. The adjusted liquid super-cell was then NVT-run for 5000 ps (N, V, and T constant in the ensemble) to extract its RDF, which was generated by VASP as part of the output of this run.

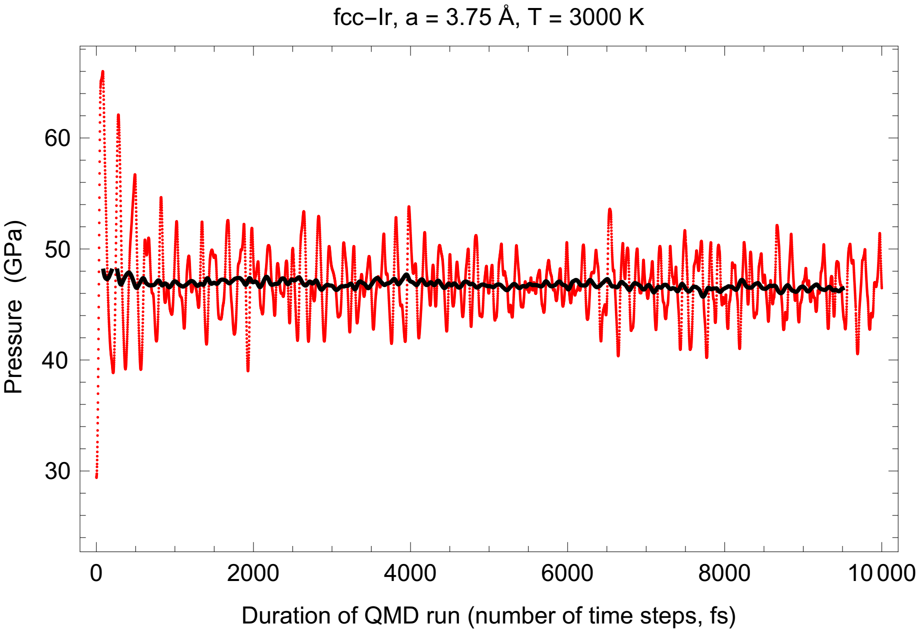

Figure 2. Time evolution of pressure during the 10,000 time step run of fcc-Ir with a lattice constant of 3.75 Å under a fixed temperature of 3000 K using the Nosé algorithm. The moving average is shown as a black line. In the vertical axis, pressure is in GPa.

3. Results

3.1. Experiments

During the experiment, several heating ramps were performed on Ir starting from two different initial pressures: 20 GPa and 30 GPa. The results obtained from the different ramps were completely comparable with each other and an example of the observed structural and textural evolution is reported in Figure 3 at selected *T*. In the investigated *P*–*T* range, only peaks belonging to *fcc* Ir and MgO were observed with no evidence of any solid–solid phase transitions or chemical reactions (such as IrO_2 or $MgIrO_3$). The texture of both MgO and Ir showed a similar temperature-induced evolution, starting with a high quality powder averaging at 300 K and showing increased recrystallization with the raising *T* (see Figure 3).

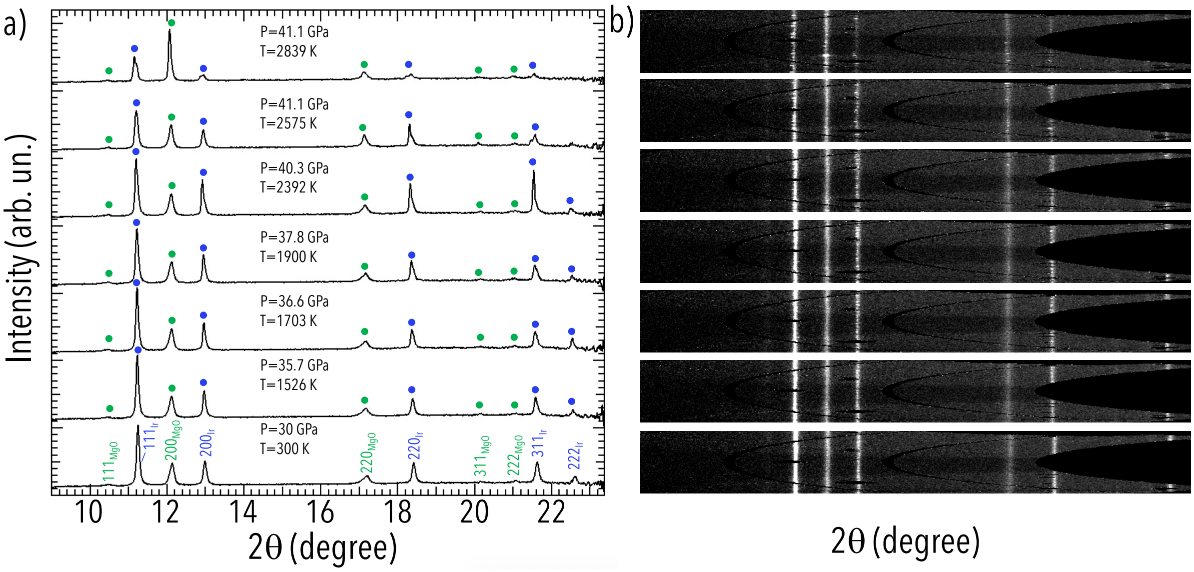

Figure 3. Selection of XRD patterns showing the (**a**) structural and the corresponding (**b**) textural evolution of an Ir sample embedded in MgO PTM between ambient *T* and 2900 K, in a pressure range between 30 GPa and 41 GPa.

During each heating ramp, a plateau in the temperature evolution was observed and, despite the continuous increase in the lasers power, it was impossible to reach higher *T*. During one particular heating ramp, together with the temperature plateau, it was possible to observe a massive diffuse XRD signal (see Figures 4 and 5), characteristic of the presence of molten material. An analysis of the textural evolution of this particular ramp (Figure 4) shows how the signal coming from the Ir sample evolves with the raising *T*: from a powder-like signal presenting several spots of higher intensities (at 1500 K) to a single-crystal-like signal caused by *T*-induced growth of the grains [18] (at 4260 K) and, finally, to a diffuse signal (at 4260 K) characteristic of the presence of liquid Ir. A better visualization of the observed behavior can be obtained from the integrated signals of the pattern reported in Figure 4. In fact, in Figure 5, it is possible to observe the amount of diffuse signal observed in the red pattern (at 2649 K) compared to the other two patterns obtained at lower *T*. Concerning the textural evolution of MgO, in Figure 4, it is possible to observe how it does not change much in the reported *T* range. This confirms that the measured liquid signal is actually from Ir and not from the insulating MgO material.

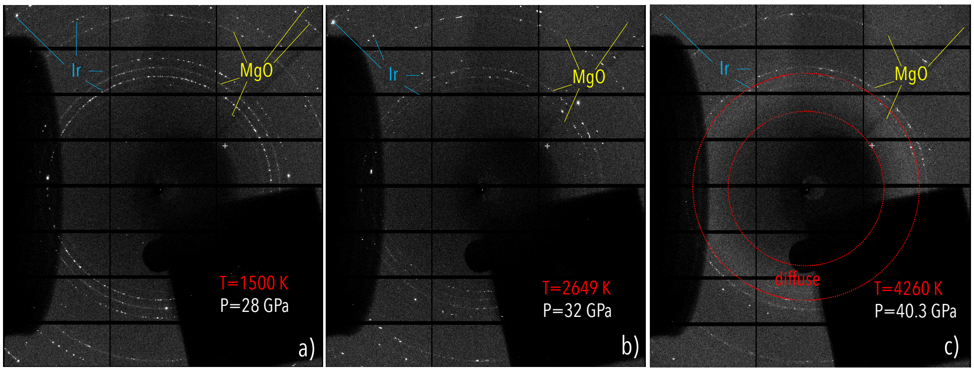

Figure 4. Textural evolution of Ir sample and MgO-insulating material during the heating ramp where melting was observed. (**a**) Both the sample and MgO are showing *T*-effects, characterized by the presence of smaller (more intense) spots withing the powder rings. (**b**) While the MgO texture remains quite similar to the previous case, Ir now exhibits the presence of single crystals caused by the growth of Ir grains [18]. (**c**) Ir crystal peaks have essentially disappeared and have now converted into an amorphous halo, whilst the XRD signal from the MgO is still similar to the previous case. In all the reported images, the peaks belonging to Ir and MgO are labelled and the corresponding *P*–*T* conditions indicated. In (**c**), the concentric red circles are used to assist the reader in identifying the presence of the diffuse halo. The shadows observed on each image are caused by the presence of the various optics of the LH system of I15 [9].

Due to the amount of liquid signal measured at 4260 K and 40.3 GPa, it was possible to extract the experimental RDF (reported as g(r) in Figure 6), obtaining confirmation of the melting of Ir and additional structural information. In particular, the two main oscillations in the RDF signal (r_1 and r_2) are found at 2.81 Å and 5.31 Å. Considering the volume expansion due to the solid/liquid transition, as expected in Ir from the slope of its Clausius–Clapeyron curve simulated by Burakovsky et al. [6,19], a value of 2.81 Å for the radius of the first coordination shell of liquid Ir is in good agreement with the first neighbour distance of 2.64 Å obtained from the last measured diffraction signal of solid Ir. Comparing the experimental and the theoretical RDF signals shown in Figure 6, it is possible to observe that both the r_1 and r_2 peaks obtained from the DFT simulation are slightly shifted towards lower r (by 0.01 nm) with respect to the experimental one. This is probably caused by the slight underestimation of volumes (therefore, of atomic distances) caused by the use of LDA (as mention above) compared to the experimental values. However, the experimental r_2/r_1 ratio of 1.87 is in good agreement with the theoretical value of 1.81 obtained from the DFT simulation. A similar value was also found for liquid Cu [20] (another *fcc* metal).

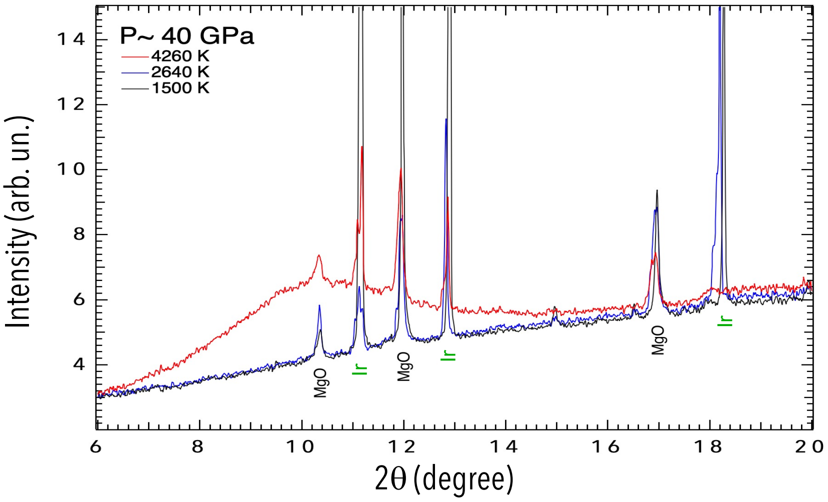

Figure 5. Integrated diffraction signal of Ir embedded in MgO at three different *T*s (the same as those reported in Figure 4), before and after the melting of Ir. In particular, the appearance of the characteristic diffuse signal from a liquid is clearly visible in the red pattern. MgO and Ir peaks are labeled.

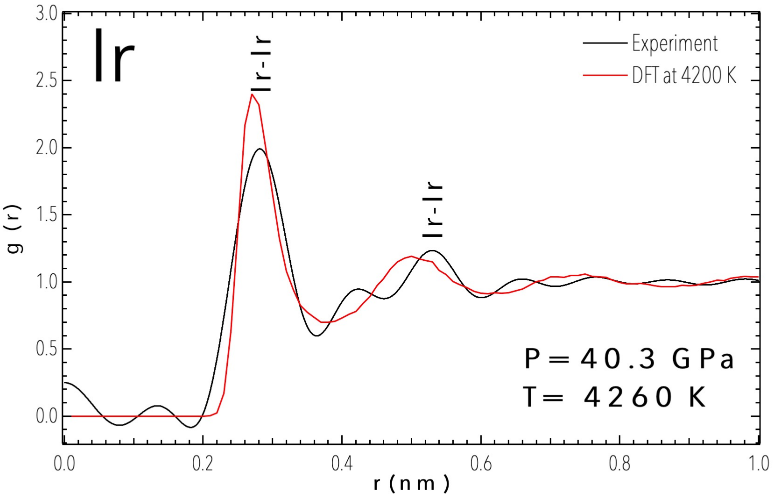

Figure 6. Comparison between the RDF signals of liquid Ir experimentally obtained at 40.3 GPa and 4260 K (black line) and the RDF signal obtained from DFT simulation at 4200 K and 40 GPa (red line).

In Figure 7, the experimental points obtained in the present study (solid and liquid) are compared to the phase boundaries calculated in Burakovsky et al. [6]. As it is possible to deduce from the figure, the present results (melting point included) are in good agreement with the previous calculation and far below the melting curve of MgO as reported in Kimura et al. [21] (confirming that the observed liquid signal is from Ir and not from the insulating material).

The unit–cell parameters of Ir at different *P*–*T* conditions were determined from a LeBail analysis of the measured XRD patterns. The present results corresponding to different isotherms are reported in Figure 8, together with the *RT* isotherms determined for experiments preformed using helium (He) [1], neon (Ne) [22], argon (Ar) [23] as pressure-transmitting media up to 140, 70, and 65 GPa, respectively. Results from *HT* experiments conducted at ambient pressure [24] are also reported in the figure for comparison.

The present *RT* results agree well with the experiments of Monteseguro et al. up to 10 GPa [1]. However, at higher pressures, they show a smaller compressibility, which becomes more similar to that determined from the experiments performed under Ar [23] and Ne [22].

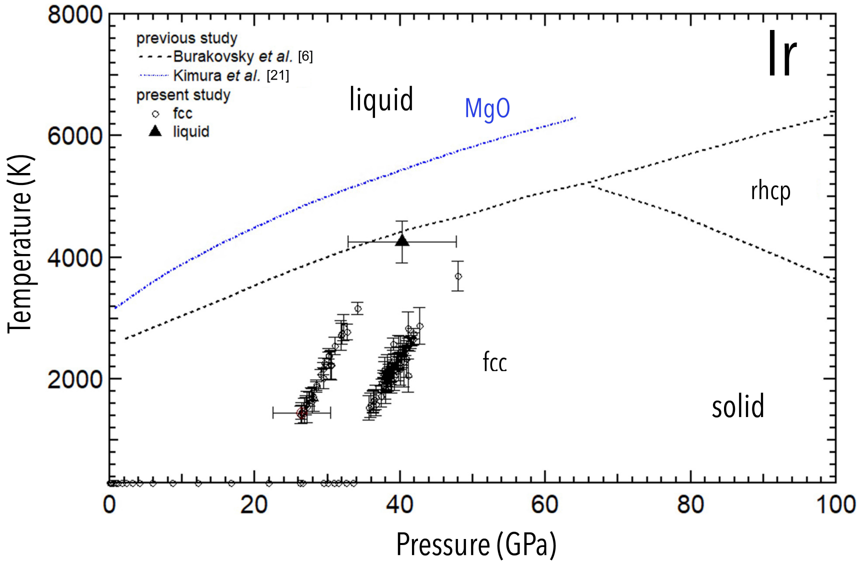

Figure 7. Ir phases as observed at the present experimental *P*–*T* conditions (solid symbols) compared to the DFT predicted phase diagram of Ir [6]. The melting line of MgO by Kimura et al. [21] is also reported for comparison. Errors in the *T* measurement are reported for all the experimental point obtained during laser heating. For simplicity, only the minimum and the maximum errors in *P* are reported for clarity reasons.

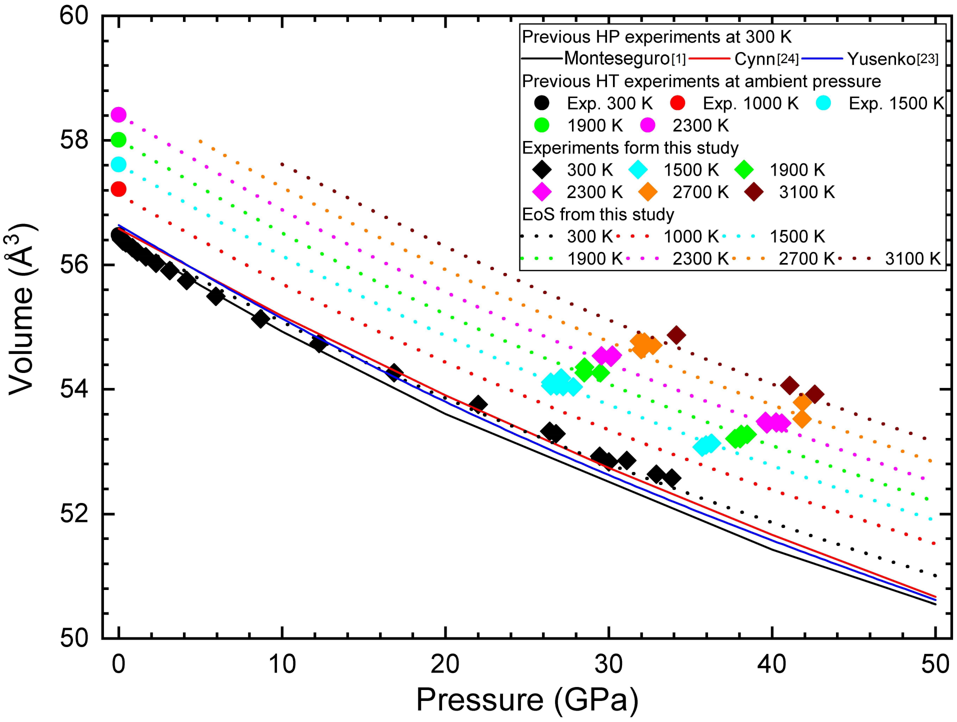

Figure 8. Unit–cell volume of Ir versus pressure for different temperatures. Diamonds correspond to the experiments of the present work. Circles are results from ambient-pressure experiments [24]. The black, blue, and red solid lines are the EoS determined from experiments carried out under He [1], Ne [22], and Ar [23]. The dashed lines are the isotherms obtained from the *P*–*V*–*T* EoS we determined.

A third-order Birch–Murnaghan (BM) equation of state [25] was fitted to the present data. The obtained volume at ambient pressure (V_0), bulk modulus (B_0), and its pressure derivative (B_0') are summarized in Table 1. They are compared with previous studies following the results from the present calculations.

Table 1. EoS parameters (at 300 K) determined from present and previous studies whose references are indicated in the center column. In the upper part, we show results from experiments indicating the pressure medium and the maximum P reached during the experiment. In the lower part, we show results from calculations.

V_0 [Å^3]	B_0 [GPa]	B_0'	Method	Pressure Medium	P Max
56.48	339 (3)	5.3 (1)	XRD [1]	Helium	140 GPa
56.58	383 (14)	3.1 (8)	XRD [23]	Argon	65 GPa
56.64 (24)	341(19)	4.7 (3)	XRD [22]	Neon	70 GPa
56.69	306 (23)	6.8 (1.5)	XRD [5]	MgO	65 GPa
56.48 (9)	360 (5)	6.0 (5)	XRD (this work)	MgO	35 GPa
56.58	366	5.0	DFT [6]		
56.17	377	5.3	DFT (this work)		

From the P–V–T data shown in Figure 8, it was possible to determine a thermal EoS taking advantage of the EosFit7 package [16]. For the analysis, we used diffraction data measured at 300 (2) K, 1500 (20) K, 1900 (20) K, 2300 (30) K, 2700 (50) K, and 3100 (50) K, as well as previous ambient-pressure results [24,26]. During the fitting procedure, the third-order BM EoS generated from the RT compression experiment was used as the isothermal part of the P–V–T EoS. In addition, a Berman equation was used as the thermal-expansion model [27], assuming a linear variation of B_0 with T. The pressure derivative of the bulk modulus was assumed to be P-independent. On the other hand, the thermal expansion was considered to be P-independent and to have a linear T-dependence. This simple model properly describes all the available experimental results, as can be seen in Figure 8. The obtained parameters are $dB_0/dT = -0.015(9)$ GPa/K, volumetric thermal expansion $\alpha = 1.6(2) \times 10^{-5}\ K^{-1}$, and $d\alpha/dT = 8.0(7) \times 10^{-10}\ K^{-2}$.

3.2. Computer Simulations

In Figure 9, the isotherms obtained from the present DFT calculations are presented and compared to the ones obtained from the experimental data (described in the previous section). According to the data reported in the figure, it is possible to observe how the present calculations underestimate the experimental volume at ambient P by less than 1%. Regarding the volumetric evolution with pressure, despite the underestimated value of V_0, at lower pressure the calculations give a slightly smaller compressibility than the experiments (larger bulk modulus). However, beyond 20 GPa and for temperatures up to 1000 K, calculations and experiment provide very similar volumetric compressions, with isotherms running nearly parallel to each other, as a consequence of the slightly smaller calculated B_0'. The *RT* EoS parameters obtained from the calculated isotherm at 300 K are summarized in Table 1. A detailed comparison with the experimental results is presented in the next section.

The calculated *HT* isotherms are well described using the same model employed to analyze the experiments. The parameters determined from the present computer simulations are $dB_0/dT = -0.03$ GPa/K, $\alpha = 1.6 \times 10^{-5}\ K^{-1}$, and $d\alpha/dT = 8.0 \times 10^{-10}\ K^{-2}$. The agreement with the experimental results is reasonably good. Only the effect of T on the bulk modulus is larger in the calculations than in the experiments, causing a stronger predicted compressibility for T higher than 1000 K. This is clearly visible in Figure 9, where the comparison of calculations with experiments shows that as both P and T go up, the theoretical p values start lagging behind their experimental counterparts; at the highest P and T of this work, the shift is as high as ≈20 GPa at 80 GPa and 3000 K.

Regarding the melting temperature, as previously discussed, the DFT calculations provide a melting curve in agreement (within the uncertainties) with the measured liquid Ir at 40 GPa. Furthermore, the calculated and the measured RDF are also in good agreement, with a difference in the position of the peaks of the first and second coordination spheres of ≈0.01 Å.

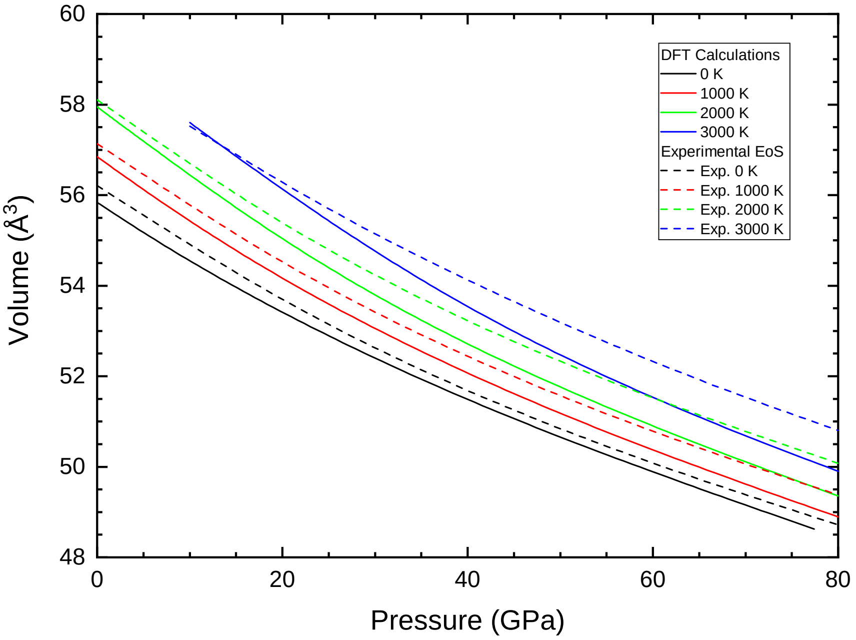

Figure 9. Calculated unit–cell volume of Ir versus *P* at different *T* (solid lines). The theoretical results are compared with the *P*–*V*–*T* EoS obtained from the experiments (dashed lines).

4. Discussion

Now we will compare the bulk modulus and its pressure derivative obtained from experiments and calculations in this work with those of the literature. Given the fact that B_0 and B_0' are correlated, a proper comparison can only be made by plotting B_0' versus B_0, as reported in Figure 10. Results from different works are included in the figure, including the error bars when available. Confidence ellipses are also represented in the figure to visualize the correlation between B_0 and B_0' of the present experiment.

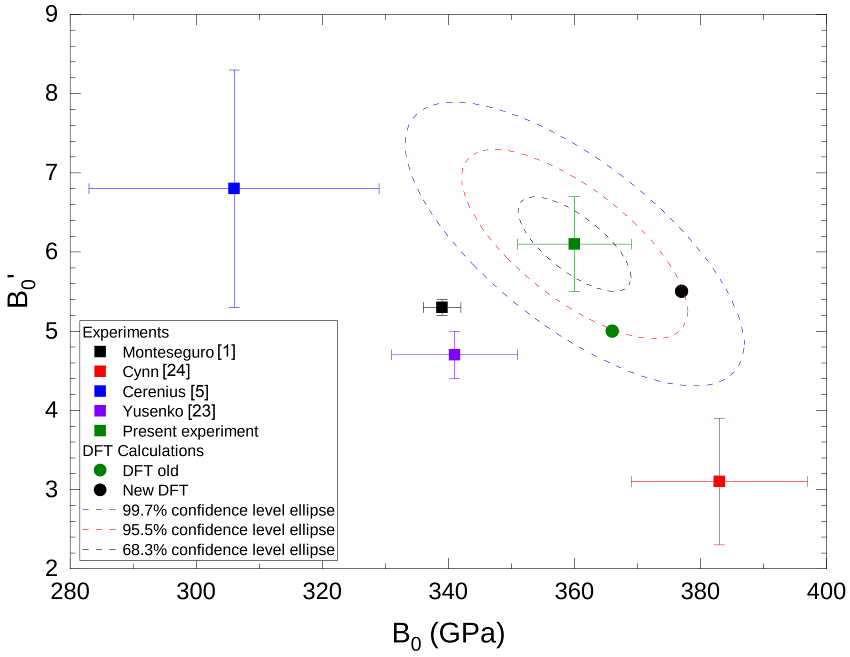

Figure 10. B_0' versus B_0. Values from different studies are included; see inset. Confidence ellipses from the present experiments are shown.

The theoretical values (from present and previous state-of-the-art calculations [6]) are within the 95.5% confidence level ellipse of the experimental ones. This means that they are only two sigmas away from the experimental results, which can be considered as a good match. The results from Monteseguro et al. [1] and Yusenko et al. [22] slightly underestimate the bulk modulus. Notice that the experiment of Monteseguro et al. [1] was done under hydrostatic conditions and in a larger pressure range. This can explain the small differences in the EoS parameters. Regarding other experiments, the results from Cynn et al. [23] overestimate B_0 and underestimate B'_0. On the other hand, the study by Cerenius et al. [5] reports an extremely low value for B_0 but a reasonable value for its pressure derivative. This could indicate a systematic error in the bulk modulus determination not affecting the pressure derivative, which could be related to the sample bridging between the two diamond anvils.

Regarding the calculations, in addition to the previous study of Burakovsky et al. [6], there were previous DFT and tight-binding calculations. Calculations using a Kleinman–Bylander separable non-local pseudopotential [28] give an overestimated bulk modulus (B_0 = 385 GPa) and the same happens for calculations using a Hartwigsen–Goedecker-Hutter semi-core potential (B_0 = 399 GPa) [29]. On the other hand, tight-binding calculations that underestimate the bulk modulus [30] give an underestimated bulk modulus (B_0 = 341 GPa).

In conclusion, Figure 10 and the comparison with previous studies show that the *RT* EoS reported here gives the most accurate description of the volumetric compression of Ir. This, and the agreement with previous studies and calculations of the thermal-expansion behavior of Ir at *HP*, reinforce confidence regarding the accurate determination of the present *P*–*V*–*T* EoS of Ir. In summary, the associated parameters are: V_0 = 56.48 (9) A^3, B_0 = 360 (5) GPa, B_0' = 6.0 (5), $dB_0/dT = -0.015(9)$ GPa/K, $\alpha = 1.6(2) \times 10^{-5}\ K^{-1}$, and $d\alpha/dT = 8.0(7) \times 10^{-10}\ K^{-2}$.

Compared to the other transition metals (such as Au, Cu, Pt, Nb, Re, Ta, etc.), which have been proposed as pressure standards in the literature [31], Ir results less compressible than most of them (with the exception of Os [32]). In fact, their bulk moduli are ranging from 136 GPa (Cu) to 320 GPa (Ru) [33–36]. However, Ir has several advantages compared to the other metals, for example, it has a much higher melting temperature than Au, Cu, and Pt [13,37,38], which makes it more suitable for *HP*–*HT* experiments. On the other hand, it is much more inert than Re, Ta, and W, making it a better candidate as standard for *HP*–*HT* experiments where chemical reactions are a sensitive issue [2,3]. In addition, the thermal expansion of Ir ($\alpha = 1.6(2) \times 10^{-5}\ K^{-1}$) is one third of that of Au and Cu [39,40] and around 30% smaller than that of Pt and Ru [33,41]. This fact makes Ir a more interesting metal for pressure calibration at *HT*, since the smaller thermal expansion makes it more accurate, providing smaller thermal pressure (being it proportional to $\alpha \times B_0$ [10]). In the case of Ir $\alpha \times B_0$ = 0.0058 GPa K^{-1}, while in Au, Cu, Pt, and Ru, the same magnitude ranges from 0.0062 to 0.0074 GPa K^{-1}. In conclusion, Ir can be considered as an ideal standard used for pressure calibration in high *P*–*T* XRD experiments due to its simple structure, phase stability, strong signal, inert chemical properties, high melting temperature, and thermal expansion properties.

5. Conclusions

In the present study, a thermal pressure–volume equation of state for iridium valid up to 80 GPa and 3100 K has been obtained combining *HP*–*HT* laser-heating powder XRD experiments and molecular-dynamic DFT calculations. The stability of the *fcc* phase of iridium was also explored experimentally, confirming it as the only solid phase observed in the investigated *P*–*T* region (48 GPa and 3100 K). The melting temperature of Ir at 40 GPa was also determined to be 4260 (200) K. Results are compared with previous experimental and theoretical studies. The reliability of the present results is supported by the consistency between the values yielded for EoS parameters by the two methods. In particular, we found that the EoS parameters determined from the present experiments agree very well with the calculated ones (within 95.5% confidence level ellipse). The experimental parameters are V_0 = 56.48 (9) A^3, B_0 = 360 (5) GPa, B_0' = 6.0 (5), $dB_0/dT = -0.015$ (9) GPa/K, $\alpha = 1.6$ (2) $\times 10^{-5}$ K^{-1}, and $d\alpha/dT = 8.0$ (7) $\times 10^{-10}$ K^{-2}. The reported results will allow the use of Ir as calibration standard for high-pressure and high-temperature experiments. The comparison with other metals (Au, Cu, Pt, Nb, Re, Ta, and Os) shows that Ir is a reliable pressure standard for high-pressures and high-temperatures DAC experiments. Finally, the radial-distribution function of liquid iridium at HP and HT has been reported for the first time. Information on the first and second coordination shells of liquid iridium is reported.

Author Contributions: D.E. conceived the experiment. S.A., R.T. and E.B. conducted the experiment. S.A. and D.E. analyzed the results. L.B. performed the theoretical calculations. The manuscript is written through contributions of all authors. All authors have given approval to the final version of the manuscript.

Funding: This work was partially supported by the Spanish Ministry of Science, Innovation, and Universities under grants PID2019-106383GB-C41 and RED2018-102612-T (MALTA Consolider-Team Network) and by Generalitat Valenciana under grant Prometeo/2018/123 (EFIMAT). R.T. acknowledges funding from the Spanish MINECO via the Juan de la Cierva Formación program (FJC2018-036185-I).

Data Availability Statement: All relevant data that support the findings of this study are available from the corresponding authors upon request.

Acknowledgments: The authors acknowledge the DLS synchrotron facilities for provision of beamtime on the beamlines I15 (DLS Ref. CY21610).

Conflicts of Interest: The authors declare no conflict of interest.

Sample Availability: Samples were obtained from a commercial supplier of high-purity metals; Goodfellow.

References

1. Monteseguro, V.; Sans, J.A.; Cuartero, V.; Cova, F.; Abrikosov, I.A.; Olovsson, W.; Popescu, C.; Pascarelli, S.; Garbarino, G.; Jönsson, H.J.M.; et al. Phase stability and electronic structure of iridium metal at the megabar range. *Sci. Rep.* **2019**, *9*, 8940. [CrossRef]
2. Chulia-Jordan, R.; Santamaria-Perez, D.; Marqueno, T.; Ruiz-Fuertes, J.; Daisenberger, D. Oxidation of High Yield Strength Metals Tungsten and Rhenium in High-Pressure High-Temperature Experiments of Carbon Dioxide and Carbonates. *Crystals* **2019**, *9*, 676. [CrossRef]
3. Errandonea, D. Observation of chemical reactions between alkaline-earth oxides and tungsten at high pressure and high temperature. *J. Phys. Chem. Solids* **2009**, *70*, 1117–1120. [CrossRef]
4. Schock, R.; Johnson, K. Compression of iridium to 175 kbar. *Fiz. Metal. Met.* **1971**, *31*, 1100.
5. Cerenius, Y.; Dubrovinsky, L. Compressibility measurements on iridium. *J. Alloys Compd.* **2000**, *306*, 26. [CrossRef]
6. Burakovsky, L.; Burakovsky, N.; Cawkwell, M.; Preston, D.; Errandonea, D.; Simak, S. Ab initio phase diagram of iridium. *Phys. Rev. B* **2016**, *94*, 094112. [CrossRef]
7. Dubrovinsky, L.; Dubrovinskaia, N.; Bykova, E.; Bykov, M.; Prakapenka, V.; Prescher, C.; Glazyrin, K.; Liermann, H.P.; Hanfland, M.; Ekholm, M.; et al. The most incompressible metal osmium at static pressure above 750 gigapascal. *Nature* **2015**, *525*, 226. [CrossRef] [PubMed]
8. Tal, A.; Katsnelson, M.; Ekholm, M.; Jnsson, H.; Dubrovinsky, L.; Dubrovinskaia, N.; Abrikosov, I. Pressure-induced crossing of the core level in 5d metals. *Phys. Rev. B* **2016**, *93*, 205150. [CrossRef]
9. Anzellini, S.; Kleppe, A.; Daisenberger, D.; Wharmby, M.; Giampaoli, R.; Boccato, S.; Baron, M.; Miozzi, F.; Keeble, D.; Ross, A.; et al. Laser-heating system for high-pressure X-ray diffraction at the extreme condition beamline I15 at Diamond Light Source. *J. Synchrotron Radiat.* **2018**, *25*. [CrossRef]
10. Anzellini, S.; Boccato, S. A Practical Review of the Laser-Heated Diamond Anvil Cell for University Laboratories and Synchrotron Applications. *Crystals* **2020**, *10*, 459. [CrossRef]
11. Benedetti, L.; Loubeyre, P. Temperature gradients, wavelength-dependent emissivity, and accuracy of high and very-high temperatures measured in the laser-heated diamond cell. *High Press. Res.* **2004**, *24*, 423–445. [CrossRef]
12. Dorogokupets, P.I.; Oganov, A.R. Ruby, metals, and MgO as alternative pressure scales: A semiempirical description of shock-wave, ultrasonic, X-ray, and thermochemical data at high temperatures and pressures. *Phys. Rev. B* **2007**, *75*, 024115. [CrossRef]
13. Anzellini, S.; Monteseguro, V.; Bandiello, E.; Dewaele, A.; Burakovsky, L.; Errandonea, D. In situ characterization of the high pressure- high temperature meltig curve of platinum. *Sci. Rep.* **2019**, *9*, 13034. [CrossRef]

14. Prescher, C.; Prakapenka, V. DIOPTAS: A program for reduction of two-dimensional X-ray diffraction data and data exploration. *High Press. Res.* **2015**, *35*, 223. [CrossRef]
15. Coelho, A. TOPAS and TOPAS-Academic: An optimization program integrating computer algebra and crystallographic object written in C++. *J. Appl. Crystallogr.* **2018**, *51*, 210. [CrossRef]
16. Angel, R.J.; Gonzalez-platas, J.; Alvaro, M. EosFit7c and a Fortran module (library) for equation of state calculations. *Z. Kristallogr.* **2014**, *229*, 405–419. [CrossRef]
17. Grabowski, B.; Wippermann, S.; Glensk, A.; Hickel, T.; Neugebauer, J. Random phase approximation up to the melting point: Impact of anharmonicity and nonlocal many-body effects on the thermodynamics of Au. *Phys. Rev. B* **2015**, *91*, 201103. [CrossRef]
18. Hrubiak, R.; Meng, Y.; Shen, G. Microstructures define melting of molybdenum at high pressure. *Nat. Commun.* **2017**, *8*, 14562. [CrossRef] [PubMed]
19. Burakovsky, L.; Cawkwell, M.; Preston, D.; Errandonea, D.; Simal, S. Recent ab initio phase diagram studies: Iridium. *J. Phys. Conf. Ser.* **2017**, *950*, 042021. [CrossRef]
20. Sukhomlinov, S.; Müser, M. A mixed radial, angular, three-body distribution function as a tool for local structure characterization: Application to single-component structures. *J. Chem. Phys.* **2020**, *152*, 194502. [CrossRef]
21. Kimura, T.; Ohfuji, H.; Nishi, M.; Irifune, T. Melting temperatures of MgO under high pressure by micro-texture analysis. *Nat. Commun.* **2017**, *8*, 15735. [CrossRef]
22. Yusenko, K.; Khandarkhaeva, S.; Fedotenko, T.; Pakhomova, A.; Gromilov, S.; Dubrovinsky, L.; Dubrovinskaia, N. Equations of state of rhodium, iridium and their alloys up to 70 GPa. *J. Alloys Compd.* **2019**, *788*, 212. [CrossRef]
23. Cynn, H.; Klepeis, J.E.; Yoo, C.S.; Young, D.A. Osmium has the Lowest Experimentally Determined Compressibility. *Phys. Rev. Lett.* **2002**, *88*, 676. [CrossRef]
24. Halvorson, J.J.; Wimber, R.T. Thermal Expansion of Iridium at High Temperatures. *J. Appl. Phys.* **1972**, *43*, 2519–2522. [CrossRef]
25. Birch, F. Elasticity and constitution of the Earth's interior. *J. Geophys. Res.* **1952**, *57*, 227–286. [CrossRef]
26. Arblaster, J. Crystallographic properties of iridium. *Platin. Met. Rev.* **2010**, *54*, 93. [CrossRef]
27. Anzellini, S.; Errandonea, D.; MacLeod, S.; Botella, P.; Daisenberger, D.; DeAth, J.; Gonzalez-Platas, J.; Ibanez, J.; McMahon, M.; Munro, K.; et al. Phase diagram of calcium at high pressure and high temperature. *Phys. Rev. Mater.* **2018**, *2*, 083608. [CrossRef]
28. Grussendorff, S.; Chetty, N.; Dreysse, H. Theoretical studies of iridium under pressure. *J. Phys. Condens. Matter* **2003**, *15*, 4217. [CrossRef]
29. Fang, H.; Liu, B.; Gu, M.; Liu, X.; Huang, S.; Ni, C.; Wang, R. High-pressure lattice dynamic and thermodynamic properties of Ir by first-principles calculations. *Physica B* **2010**, *405*, 732. [CrossRef]
30. Gheribi, A.E.; Roussel, J.M.; Rogez, J. Phenomenological Hugoniot curves for transition metals up to 1 TPa. *J. Phys. Condens. Matter* **2010**, *19*, 476218. [CrossRef]
31. Sokolova, T.S.; Dorogokupets, P.I.; Dymshits, A.M.; Danilov, B.S.; Litasov, K.D. Microsoft excel spreadsheets for calculation of P–V–T relations and thermodynamic properties from equations of state of MgO, diamond and nine metals as pressure markers in high-pressure and high-temperature experiments. *Comput. Geosci.* **2016**, *94*, 162–169. [CrossRef]
32. Takemura, K. Bulk modulus of osmium: High-pressure powder X-ray diffraction experiments under quasihydrostatic conditions. *Phys. Rev. B* **2004**, *70*, 012101.
33. Anzellini, S.; Errandonea, D.; Cazorla, C.; MacLeod, S.; Monteseguro, V.; Boccato, S.; Bandiello, E.; Anichtchenko, D.D.; Popescu, C.; Beavers, C. Thermal equation of state of ruthenium characterized by resistively heated diamond anvil cell. *Sci. Rep.* **2020**, *10*, 7092. [CrossRef] [PubMed]
34. Dewaele, A.; Loubeyre, P.; Mezouar, M. Equations of state of six metals above 94 GPa. *Phys. Rev. B* **2004**, *094112*, 1–8.
35. Anzellini, S.; Dewaele, A.; Occelli, F.; Loubeyre, P.; Mezouar, M. Equation of state of rhenium and application for ultra high pressure calibration. *J. Appl. Phys.* **2014**, *115*, 043511, [CrossRef]
36. Errandonea, D.; Burakovsky, L.; Preston, D.E.A. Experimental and theoretical confirmation of an orthorhombic phase transition in niobium at high pressure and temperature. *Commun. Mater.* **2020**, *1*, 60, [CrossRef]
37. Weck, G.; Recoules, V.; Queyroux, J.; Datch, F.; Bouchet, J.; Ninet, S.; Garbarino, G.; Mezouar, M.; Loubeyre, P. Determination of the melting curve of gold up to 110 GPa. *Phys. Rev. B* **2020**, *101*, 014106. [CrossRef]
38. Dewaele, A.; Mezouar, M.; Guignot, N.; Loubeyre, P. Melting of lead under high pressure studied using second-scale time-resolved X-ray diffraction. *Phys. Rev. Condens. Matter Mater. Phys.* **2007**, *76*, 1–5. [CrossRef]
39. Dorogokupets, P.I.; Dewaele, A. Equations of state of MgO, Au, Pt, NaCl-B1, and NaCl-B2: Internally consistent high-temperature pressure scales. *High Press. Res.* **2007**, *27*, 431–446. [CrossRef]
40. Wang, Y.; Zhang, J.; Xu, H.; Lin, Z.; Daemen, L.L.; Zhao, Y.; Wang, L. Thermal equation of state of copper studied by high P-T synchrotron X-ray diffraction. *Appl. Phys. Lett.* **2009**, *94*, 071904. [CrossRef]
41. Zha, C.S.; Mibe, K.; Bassett, W.A.; Tschauner, O.; Mao, H.K.; Hemley, R.J. P-V-T equation of state of platinum to 80 GPa and 1900 K from internal resistive heating/X-ray diffraction measurements. *J. Appl. Phys.* **2008**, *103*, 054908. [CrossRef]